Structure and Electrochemistry of $LiNi_{1/3}Co_{1/3-y}M_yMn_{1/3}O_2$ (M=Ti, Al, Fe) Positive Electrode Materials

James Wilcox[a,b], Sébastien Patoux[c], and Marca Doeff [a]

a) Materials Sciences Division

b) Department of Materials Science and Engineering

University of California

Berkeley, CA 94720

c) Commissariat a l'Energie Atomique (CEA) /

Laboratoire d'Innovation pour les Technologies des Energies Nouvelles

38054 Grenoble Cedex 9, France

* mmdoeff@lbl.gov

Abstract

A series of materials based on the $LiNi_{1/3}Co_{1/3-y}M_yMn_{1/3}O_2$ (M=Ti, Al, Fe) system have been synthesized and examined structurally and electrochemically. It is found that the changes in electrochemical performance depend highly on the nature of the substituting atom and its effect on the crystal structure. Substitution with small amounts of Ti^{4+} (y=1/12) leads to the formation of a high capacity and high rate positive electrode material. Iron substituted materials suffer from an increased anti-site defect concentration and exhibit lower capacities and poor rate capabilities. Single-phase materials are found for $LiNi_{1/3}Co_{1/3-y}Al_yMn_{1/3}O_2$ when $y \leq 1/4$ and all exhibit decreased

capacities when cycled to 4.3V. However, an increase in rate performance and cycle stability upon aluminum substitution is correlated with an improved lamellar structure.

Introduction

A significant amount of research has been directed at finding positive electrode materials with high capacity as well as low cost and toxicity to replace $LiCoO_2$. Of particular interest is the series of materials, $LiNi_{1-y-z}Co_yMn_zO_2$, which potentially combine the rate performance of $LiCoO_2$, the high capacity of $LiNiO_2$, and the structural stabilization imparted by the presence of Mn^{4+}.[1, 2] Specifically, $LiNi_{1/3}Co_{1/3}Mn_{1/3}O_2$ has garnered much attention and has been shown to deliver 150 mAh/g between 2.5 and 4.2 V versus lithium and close to 200 mAh/g when the charge potential limit is increased to 4.6 volts.[3-7] In addition, $LiNi_{1/3}Co_{1/3}Mn_{1/3}O_2$ possesses excellent power characteristics, exceeding the high power pulse requirement for hybrid vehicle applications,[8] and increased thermal abuse tolerance compared to $LiNi_{0.8}Co_{0.15}Al_{0.05}O_2$.[9]

The inherent improvements in rate capability of $LiNi_{1/3}Co_{1/3}Mn_{1/3}O_2$ over other oxide materials, including $LiNi_{0.5}Mn_{0.5}O_2$ produced using traditional methods,[10-12] is due largely to the structural properties associated with the presence of cobalt. AMO_2 type materials with the highly layered α-$NaFeO_2$ structure (space group $R\bar{3}m$), where A is typically Li^+ and M is a metal 3+ cation, are stabilized for metal ions with an ionic radius substantially smaller than that of lithium (0.76 Å).[13, 14] Due to the small ionic radius of low spin Co^{3+} (0.545 Å) the incorporation of cobalt into the crystal lattice minimizes anti-site cation defect concentrations leading to facile lithium ion transport.[14-18]

To create electrode materials with further reduced cobalt contents and lower anti-site defect concentrations, while avoiding effective but complicated ion exchange pathways,[19] substitutive elements should promote the formation of a lamellar structure through either steric or chemical interactions. Iron, which has an ionic radius of 0.645 Å in the low spin state, is an attractive replacement for cobalt due to its low cost and toxicity. However, the native lithiated oxide, $LiFeO_2$, is not layered like α-$NaFeO_2$ but has an ordered tetragonal structure (γ-$LiFeO_2$, space group $I4_1/amd$).[20, 21] Accordingly, substitution into the layered oxide materials has been limited to relatively low levels. $LiNi_{1/3}Co_{1/6}Fe_{1/6}Mn_{1/3}O_2$, synthesized using a sol-gel synthesis method delivers approximately 150 mAh/g between 3.0 and 4.5 V vs. Li/Li^+ although a ~20% capacity fade within the first 30 cycles was observed.[22]

A previous report on the selective replacement of cobalt with aluminum in the series $LiNi_{1/3}Al_{1/3-x}Co_xMn_{1/3}O_2$ indicates that single phase materials are formed for $1/6 \leq x \leq 1/3$.[23] Interestingly, even given the small ionic radius of the Al^{3+} ion (0.545 Å), an increase in the cation mixing was observed. This was connected with an increased cell polarization and limited capacity below 4.5 V (~120 mAh/g at x=0).

Several different titanium substituted layered oxides have been reported in the literature including $LiCo_{1-z}Ti_zO_2$ (z=0.25, 0.5),[24] $LiNi_{1-x}Ti_xO_2$ ($0 \leq x \leq 0.1$, 0.5),[25, 26] $LiNi_{0.8-y}Ti_yCo_{0.2}O_2$ ($0 \leq y \leq 0.1$),[27] and $LiNi_{0.8}Ti_{0.1}Co_{0.1}O_2$.[28] In most cases, it was found that the incorporation of titanium leads to improved reversibility and thermal stability. The structural effects of titanium substitution remain unclear however, with both increasing and decreasing anti-site defect concentrations being reported. This is not surprising, as depending on the chemistry involved, substitution with Ti^{4+} may lead to the formation of

a Ni^{2+} component for charge compensation. Divalent nickel has a strong propensity to migrate to the lithium *3b* site and may account for at least some of the disparities reported experimentally.

The goal of this work is to understand the systematic changes caused by substitution of Fe^{3+}, Al^{3+}, and Ti^{4+} for Co^{+3} in $LiNi_{1/3}Co_{1/3-y}M_yMn_{1/3}O_2$, for compositions leading to single-phase materials. The effect of these substitutions on the crystallographic parameters, cycle life, and rate performance are discussed.

Experimental

The glycine nitrate combustion (GNC) process was used for the synthesis of all oxide active materials used in this study.[29, 30] Aqueous solutions of $LiNO_3$ (Mallinckrodt), $Mn(NO_3)_2$ (45-50 wt.% in dilute nitric acid, Sigma Aldrich), $Co(NO_3)_2$-$6H_2O$ (98%, Sigma Aldrich), $Ni(NO_3)_2 \cdot 6H_2O$ (Sigma Aldrich), $Al(NO_3)_3 \cdot 9H_2O$ (98+%, Sigma Aldrich), $Fe(NO_3)_3 \cdot 9H_2O$ (98% EMD), and $TiO(NO_3)_2$ and glycine (98.5+%, Sigma Aldrich) corresponding to the desired stoichiometry were combined in a stainless steel combustion chamber. The solution was then concentrated on a hot plate until auto ignition occurred. $TiO(NO_3)_2$ was prepared via the hydrolysis of $TiCl_4$ (99.9%, Sigma Aldrich) with ammonia and subsequent reaction with nitric acid (69%, BDH).[31] For comparison purposes, a constant glycine to nitrate ratio of 0.5 was used for all materials corresponding to a combustion temperature of about 1350° C.[29] After combustion, powders were planetary ball milled for one hour in acetone and dried under flowing nitrogen before being fired at 800° C (4° C/min heating rate) for four hours in air.

Powder X-ray diffraction (XRD) was performed on a Phillips X'Pert diffractometer with an X'celerator detector using Cu Kα radiation. A back loading powder holder was used to minimize the impact of any preferred orientation. Unit cell parameters were obtained from Rietveld refinement using the WINPLOTR/FullProf suite. [32] Particle morphology studies were conducted using a field emission-scanning electron microscope (FESEM, Jeol JSM-6340F).

Laminate composite electrodes comprised of 84 wt.% active material, 8 wt.% poly(vinylidine fluoride) (PVDF, Kureha Chemical Ind. Co. Ltd.), 4 wt.% compressed acetylene black, and 4 wt.% SFG-6 synthetic flake graphite (Timcal Ltd., Graphites and Technologies) were prepared by applying slurries in 1-methyl-2-pyrrolidinone onto carbon coated current collectors (Intelicoat Technologies) by automated doctor blade. After drying in air and in vacuum for at least 24 hours, 1.8 cm^2 electrodes having an average loading of 7-10 mg/cm^2 of active material were punched out. Coin cells (2032) were assembled in a helium filled glove box with lithium metal anodes and 1M $LiPF_6$ in 1:2 ethylene carbonate/dimethyl carbonate (EC/DMC) electrolyte solution (Ferro). Galvanostatic cycling was carried out on an Arbin BT/HSP-2043 cycler between limits of 2.0 and 4.3-4.7V. All cells were charged at a current density of 0.1 mA/cm^2 independent of the discharge rate.

Results and Discussion

The impact of substitution for cobalt in layered oxide systems upon electrochemical performance will vary depending on the nature of the substituting atom. Because cobalt does not become electroactive until potentials exceeding 4.3 V, much of

the capacity related to the $Co^{3+/4+}$ redox couple is not utilized under normal cycling conditions.[33, 34] Therefore, the effect on practical capacities should be minimal as long as no other properties, such as ionic or electronic conductivity or voltage characteristics, are grossly affected by the substitution. This is significant as it may allow for the substitution of cobalt with electrochemically inactive species such as Al^{+3} that lower the theoretical capacity (e.g., 208 mAh/g for $LiNi_{1/3}Al_{1/3}Mn_{1/3}O_2$) compared to the parent material, $LiNi_{1/3}Co_{1/3}Mn_{1/3}O_2$ (278 mAh/g). Aliovalent substitution with Ti^{+4} requires the reduction of the redox state of another transition metal species to maintain charge neutrality. The most probable charge balance reaction is partial reduction of Mn^{4+} to Mn^{3+}. Mn^{3+} is electroactive in the window of 3-3.5 V,[35] and can compensate for the inactivity of Ti^{4+}. Therefore a slight increase in theoretical capacity is expected (289 mAh/g for the hypothetical $LiNi_{1/3}Ti_{1/3}Mn_{1/3}O_2$ due to the lower atomic weight of Ti compared to Co. (It may, however, be difficult to detect Mn electroactivity at the low substitution levels utilized in this study).[25] Iron substituted materials have slightly higher theoretical capacities (e.g., 281 mAh/g for the hypothetical $LiNi_{1/3}Fe_{1/3}Mn_{1/3}O_2$) than the $LiNi_{1/3}Co_{1/3}Mn_{1/3}O_2$ because of the slightly lower atomic weight of iron and its presumed electroactivity.

In this study, single-phase materials were obtained for all substitutions when y was limited to a value of 1/12 in $LiNi_{1/3}Co_{1/3-y}M_yMn_{1/3}O_2$ (M=Ti, Al, Fe). Substitution of titanium and iron at levels greater than 1/12 leads to the formation of spinel-like impurity phases and will not be further discussed. A higher degree of solubility was observed in the aluminum substituted system where an impurity phase was observed only for y=1/3 in this study.

The primary particle size estimated from Rietveld refinement is approximately 40-50 nm for all samples and agrees well with the particle size (50 nm) observed in transmission electron microscope images of similarly produced oxide powders.[30] Figure 1 shows an SEM image of the parent material, $LiNi_{1/3}Co_{1/3}Mn_{1/3}O_2$, produced using the glycine nitrate combustion method and is characteristic of all of the materials used in this study. The agglomeration into secondary particles with a diameter of approximately 500 nm can be seen clearly and is also typical of all the materials used in this study.

$LiNi_{1/3}Co_{1/4}M_{1/12}Mn_{1/3}O_2$ (M=Co, Ti, Al, Fe)

The X-ray powder diffraction patterns presented in Figure 2 indicate that the substitution of 1/12 of the cobalt content with aluminum, iron, or titanium results in highly crystalline single-phase powders. All peaks could be indexed in the $R\bar{3}m$ space group with no evidence of a second phase (the 200 peak of the aluminum sample holder is, however, evident in the patterns). The results of the Rietveld refinements are presented in Table 1. For the α-$NaFeO_2$ structure, the *a* lattice parameter is a measure of the distance between metal centers in the transition metal plane and is relatively unaffected by substitution; only a small shift (0.4% maximum) is observed. The experimentally observed trend is readily explained by the minor differences in ionic radii of cobalt (0.545 Å), aluminum (0.535 Å), titanium (0.605 Å), and iron (0.645 Å).[13] Minor shifts in the *c*-axis are observed upon substitution; the *c* lattice parameter expands to a maximum of 14.298 Å (0.3 %) upon substitution with the largest ion (Ti).

The overlap of the 200 peak from the aluminum sample holder with the 104 peak of the x-ray patterns in Figure 2 precluded the implicit refinement of the anti-site defect concentration, but the *c/3a* ratio has been shown to be a close corollary for many

materials.[36] The ideal structure with a cubic close packed framework has a value of 1.633. For materials with the α-$NaFeO_2$ structure, this ratio increases significantly, approaching 1.793 for an ideal layered material with no ion-mixing, such as $LiTiS_2$.[37] $LiNi_{1/3}Co_{1/3}Mn_{1/3}O_2$ has a *c/3a* ratio of 1.660, implying a significant degree of cation mixing. Substitution with aluminum (1.663) and titanium (1.661) leads to an increase in this value and, presumably, reduced anti-site defect content. In contrast, the *c/3a* ratio of $LiNi_{1/3}Co_{1/4}Fe_{1/12}Mn_{1/3}O_2$ (1.656) is lower than that of the parent compound. This reflects the tendency of materials with high iron content to crystallize in the γ-$LiFeO_2$ structure, with an ordered arrangement of lithium and iron on the *3a* and *3b* crystallographic sites rather than in a lamellar structure. While large shifts in the c/3a ratio can generally be ascribed to changes in the anti-site defect concentration, the dimension of the transition metal layer may also change upon substitution with an ion that is different in size than the original. However, the ionic radii of low spin Fe^{3+}, Al^{3+}, and Ti^{4+} are not substantially different than that of Co^{3+}, so that the c/3a ratio is expected to reflect primarily changes in the anti-site defect concentrations in these materials.

$Li/LiNi_{1/3}Co_{1/4}M_{1/12}Mn_{1/3}O_2$ (M=Co, Ti, Al, Fe) cells cycled at low current densities (0.1 mA/cm^2) between 2.0 and 4.3 V (Figure 3) show that substitution of even small amounts of cobalt in $LiNi_{1/3}Co_{1/3}Mn_{1/3}O_2$ has a dramatic effect on the electrochemical performance. Cells containing the parent material or $LiNi_{1/3}Co_{1/4}Ti_{1/12}Mn_{1/3}O_2$ deliver ~170 mAh/g on the first discharge and cycle with negligible capacity fade. $Li/LiNi_{1/3}Co_{1/4}Al_{1/12}Mn_{1/3}O_2$ cells cycle equally well, but the discharge capacity is decreased by about 11%. $Li/LiNi_{1/3}Co_{1/4}Fe_{1/12}Mn_{1/3}O_2$ cells only deliver 142 mAh/g initially and the capacity fades rapidly at a rate of 0.6%/cycle. This is

similar to previous findings on the effect of Fe substitution in layered transition metal oxides.[21] XPS experiments and *ab-initio* calculations have shown that iron is electroactive in the same potential window as the $Ni^{2+/4+}$ redox couple.[22] Therefore, the reduced practical capacity is assumed to be a result of kinetic rather than thermodynamic limitations.

Differential capacity plots of the first cycles of the $Li/LiNi_{1/3}Co_{1/4}M_{1/12}Mn_{1/3}O_2$ (M=Co, Ti, Al, Fe) cells are presented in Figure 4. All of the dQ/dV plots for the substituted materials show increases in the peak charge and discharge potentials and broader peaks compared to those of the parent compound, indicating that the voltage profiles are modified. This not only serves as a strong indicator that the substitutive elements were incorporated into the host lattice but also shows the effects on the electrochemical potential of lithium ion insertion and removal. The shift is greatest for the Al-substituted material (approximately 50 mV) and has been predicted by *ab-initio* calculations.[23, 38-40] In general, the increase in discharge peak potential is less pronounced than for charge, with all of the substituted materials delivering peak capacity near 3.77 V compared to 3.75 V for the unsubstituted analog. The increase in charge potential explains the lower-than-expected practical capacities obtained for several of the substituted materials using a 4.3V cutoff. Increasing the charge cutoff potential to 4.7 V allows significantly higher utilization of the electrode active materials (Figure 5), but also results in faster capacity fading, due either to instability of the oxidized active materials or irreversible oxidation of the electrolyte solutions.

The capacities of $Li/LiNi_{1/3}Co_{1/4}M_{1/12}Mn_{1/3}O_2$ (M=Co, Ti, Al, Fe) cells as a function of current density are shown in Figure 6. Interestingly, substitution with Al or

Ti leads to improved rate capability compared to $LiNi_{1/3}Co_{1/3}Mn_{1/3}O_2$, particularly at higher current densities. The performance of $LiNi_{1/3}Co_{1/4}Ti_{1/12}Mn_{1/3}O_2$ is particularly notable, delivering ~95 mAh/g at 6 mA/cm^2 (~3C rate). The main structural difference between $LiNi_{1/3}Co_{1/3}Mn_{1/3}O_2$ and $LiNi_{1/3}Co_{1/4}Ti_{1/12}Mn_{1/3}O_2$ is the increase in the *c* parameter and lithium interslab space caused by partial replacement of Co^{3+} with the Ti^{4+} ion. The increased lithium slab dimension leads to enhanced Li ion diffusion through the adjacent tetrahedral vacancy.[15] In contrast, cells with $LiNi_{1/3}Co_{1/4}Fe_{1/12}Mn_{1/3}O_2$ have very poor rate performance with a pronounced reduction in delivered capacity upon even minor increases in the discharge current density.

Figure 7 shows first cycles of lithium cells containing $LiNi_{1/3}Co_{1/4}M_{1/12}Mn_{1/3}O_2$, (M=Co, Ti, Al, Fe) at 0.1 mA/cm^2. The irreversible capacity, defined as the difference in first charge and discharge capacity with respect to the discharge capacity, varies with the nature of the substituent and is lowest for M=Co and highest for M=Fe. High irreversible capacities are undesirable as they can considerably reduce practical energy densities. In non-stoichiometric lithium nickel oxides ($Li_{1-z}Ni_{1+z}O_2$) large irreversible capacities have been associated with the oxidation of Ni^{2+} ions residing within lithium layers. The oxidation of the extra nickel ions leads to the local collapse of the lithium layer inhibiting the re-intercalation of adjacent lithium vacancies except at very low rates.[41, 42] Choi and Manthiram suggest that a parasitic reaction between the active material and electrolyte may be responsible for the irreversibility in cells containing $LiNi_{1/3}Co_{1/3}Mn_{1/3}O_2$.[43] In the same system, Tsai et al. discovered a correlation between irreversible capacity and the inability to reduce all of the Ni^{4+} to Ni^{2+} using X-ray absorption near-edge spectroscopy (XANES).[34] Alternatively, a sudden decrease in lithium ion mobility at the end of

discharge has been observed in $LiNi_{1-y}Fe_yO_2$ materials.[44] An associated drop in potential inhibits the complete reinsertion of lithium into the structure, although an over-lithiated surface phase may be formed at potentials near 2 V.

The irreversible capacities observed for mixed metal systems are dependent upon the voltage limits used and synthesis method, and can vary substantially for identical compositions. For example, a 12.9% irreversible capacity is observed in cells with $LiNi_{1/3}Co_{1/3}Mn_{1/3}O_2$ materials produced via oxalate co-precipitation[1] but only 7% for the material in this study, typical of those made by glycine-nitrate combustion.[45] Titanium substitution does not change this significantly, but aluminum-containing materials suffer from a 13% loss in capacity during the first cycle. The irreversible capacity of the iron substituted material increases to 23% possibly reflecting the inhibited kinetics associated with the decreased *c/3a* ratio of this material and the oxidation of Ni^{2+} in the lithium layers.

Cycling cells to 4.7 V results in a substantial increase in irreversible capacity for all of the positive electrode materials. In cells containing $LiNi_{1/3}Co_{1/3}Mn_{1/3}O_2$, it doubles to 14%, while there is a nearly three-fold increase to 23% for those with $LiNi_{1/3}Co_{1/4}Ti_{1/12}Mn_{1/3}O_2$, and 31% for $LiNi_{1/3}Co_{1/4}Fe_{1/12}Mn_{1/3}O_2$. Interestingly, for Li/ $LiNi_{1/3}Co_{1/4}Al_{1/12}Mn_{1/3}O_2$ cells, there is a relatively small increase in irreversible capacity from 13% using a 4.3 V cutoff to just 17% using 4.7 V. In all cases no evidence of second phase formation between 2 and 4.3 or 4.7 V was observed.

$LiNi_{1/3}Co_{1/3-y}Al_yMn_{1/3}O_2$, $(1/3 \geq y \geq 0)$

XRD powder diffraction patterns (Figure 8) show that highly crystalline, single-phase materials are formed for aluminum contents between $0 \leq y \leq 1/4$. For y=1/3, a second

phase of γ-$LiAlO_2$ is detected, consistent with both previous experimental work [23] and as predicted by Buta et. al using *ab initio* methods[46] for materials synthesized above 600° C. Refinement of the X-ray patterns indicate that aluminum substitution has a negligible effect on the *a* unit cell parameter but that there is a systematic expansion of the *c* unit cell parameter with increasing aluminum contents (Table 1). Correspondingly, the *c/3a* ratio increases to 1.665 at y=1/3 (1.664 for the single phase material at y=1/4) indicating an improved lamellar structure upon the incorporation of aluminum. This is further substantiated by the increased splitting between the 018 and 110 peaks in the XRD patterns and the shifts in the 003 peaks (Figure 8 insets). The lithium slab dimension increases from 2.59 Å at y=0 to 2.66 Å at y=1/3 implying that the incorporation of aluminum leads to a decrease in the anti-site defect concentration.[47]In contrast, Hu *et. al*[23] observed an increase in anti-site cation defects at elevated aluminum contents. However, the materials in this study were heated to 800° C for a relatively short time (4 hours) rather than 900° C. At the higher temperature, there is reduced solubility of aluminum[46] and more substantial mixing between lithium in the *3b* site and transition metals in the *3a* position.

The discharge capacities of $Li/LiNi_{1/3}Co_{1/3-y}Al_yMn_{1/3}O_2$ ($0 \leq y \leq 1/3$) cells cycled between 2.0 and 4.3 V at a low current density (0.1 mA/cm^2) are presented in Figure 9. There is a systematic decrease in the specific capacity as the Al content is increased, as found previously.[23] The source of this phenomenon becomes apparent when looking at the differential capacity plots (Figure 10). Upon Al substitution there is a rise in the oxidation potential, as predicted by first principle calculations, due to the increased oxygen participation in the redox reaction.[40] At y=1/3, the peak oxidation potential is

located at 3.97 V and is ~200 mV greater than for the parent compound (3.75 V). Thus the potential required to remove a significant fraction of the lithium from the Al-substituted materials is above the electrolyte oxidative stability threshold of about 4.3V vs. Li/Li^+, resulting in reduced practical capacity.

Cycling to 4.7 V leads to higher capacities for all the cells containing $LiNi_{1/3}Co_{1/3-y}Al_yMn_{1/3}O_2$, ($0 \leq y \leq 1/3$) electrodes (Figure 11), although the amount of improvement is dependent upon the exact composition. For example, there is an increase of only 4% for cells containing $LiNi_{1/3}Co_{1/6}Al_{1/6}Mn_{1/3}O_2$ active materials when cycling to 4.7 (145 mAh/g) rather than 4.3 V (139 mAh/g). The higher oxidation potential has a more pronounced effect at all other substitution levels with y=0 (206 mAh/g) delivering 21% more capacity, y=1/12 (192 mAh/g) 32%, y=1/4 (136 mAh/g) 12%, and y=1/3 (123 mAh/g) 24%. Utilization is increased to 74% of the theoretical capacity for materials with $y<1/6$ cycled to 4.7V. However, for materials with $y \geq 1/6$ this decreases to 60%, reflecting the shift in the voltage profile caused by the increased Al content. Although capacity and utilization are lower, the cycling behavior improves. At substitution levels of $y \geq 1/6$ virtually no capacity fade is observed after the first cycle. The increased cycling stability may be due, in part, to the inability to completely remove all of the lithium from the structure even at high potentials. While this lowers the energy density of these materials, it is compensated in part by the increased average cell potential and has been shown to improve the thermal stability of the delithiated oxide.[36, 48, 49]

As the rate data presented in Figure 12 shows, the reduced anti-site defect concentration and increase in the Li slab dimensions (Table 1) associated with Al substitution leads to positive electrode materials with better rate capabilities than the

parent compound. All of the $LiNi_{1/3}Co_{1/3-y}Al_yMn_{1/3}O_2$ compounds retain a significantly greater portion of the discharge capacity obtained at low rates when the current is increased, independent of the value of y. However, the decreased capacity obtained below 4.3V means that the advantages are most evident only for low substitution levels and high current densities. In addition, the increase in first cycle irreversible capacity seen in Li cells as the Al content in $LiNi_{1/3}Co_{1/3-y}Al_yMn_{1/3}O_2$ is raised (Figure 13) also suggests that y should be kept low for the ideal high rate, high energy system.

Conclusions

Several new materials based on the $LiNi_{1/3}Co_{1/3-y}M_yMn_{1/3}O_2$ (M=Co, Ti, Al, Fe) system have been synthesized using the glycine nitrate combustion method. The electrochemical behavior in lithium cells of electrodes based on these materials are substantially altered compared to the $LiNi_{1/3}Co_{1/3}Mn_{1/3}O_2$ parent. These differences can be directly attributed to changes in the structural characteristics induced by the substitutions. $LiNi_{1/3}Co_{1/4}Fe_{1/12}Mn_{1/3}O_2$ exhibits lower capacity and poorer rate capabilities due to kinetic limitations resulting from an increase in the anti-site cation defect concentration as implied by a reduced *c/3a* ratio. Phase pure $LiNi_{1/3}Co_{1/3-y}Al_yMn_{1/3}O_2$ compounds are formed for $0 \leq y \leq 1/4$ but a γ-$LiAlO_2$ impurity is observed for y=1/3. Although Al substitution results in decreased capacity between 4.3 and 2.0 V when electrodes are discharged in lithium cells, capacity retention and rate capability is substantially improved. This can be attributed to decreased anti-site mixing and an increased Li slab dimension compared to $LiNi_{1/3}Co_{1/3}Mn_{1/3}O_2$. $LiNi_{1/3}Co_{1/4}Ti_{1/12}Mn_{1/3}O_2$

is particularly noteworthy as a high capacity, high rate positive electrode material with good stability and very low irreversible capacity loss.

Acknowledgment

This work was supported by the Assistant Secretary for Energy Efficiency and Renewable Energy, Office of Vehicle Technologies of the U.S. Department of Energy under Contract No. DE-AC02-05CH11231.

References

1. T.-H. Cho, Y. Shiosaki and H. Noguchi, *Journal of Power Sources*, **159**, 1322 (2006).

2. J. P. B. Ammundsen, *Advanced Materials*, **13**, 943 (2001).

3. N. Yabuuchi, Y. Koyama, N. Nakayama and T. Ohzuku, *J. Electrochem. Soc.*, **152**, A1434 (2005).

4. T. Ohzuku and Y. Makimura, *Chemistry Letters*, 642 (2001).

5. N. Yabuuchi and T. Ohzuku, *Journal of Power Sources*, **119-121**, 171 (2003).

6. Y. Koyama, N. Yabuuchi, I. Tanaka, H. Adachi and T. Ohzuku, *J. Electrochem. Soc.*, **- 151** (2004).

7. N. Yabuuchi, Y. Makimura and T. Ohzuku, *J. Electrochem. Soc.*, **154**, A314 (2007).

8. I. Belharouak, Y. K. Sun, J. Liu and K. Amine, *Journal of Power Sources*, **123**, 247 (2003).

9. I. Belharouak, W. Q. Lu, D. Vissers and K. Amine, *Electrochem. Commun.*, **8**, 329 (2006).

10. Z. H. Lu, L. Y. Beaulieu, R. A. Donaberger, C. L. Thomas and J. R. Dahn, *J. Electrochem. Soc.*, **149**, A778 (2002).

11. T. Ohzuku and Y. Makimura, *Chemistry Letters*, 744 (2001).

12. Y. Makimura and T. Ohzuku, *Journal of Power Sources*, **119**, 156 (2003).

13. R. D. Shannon, *Acta Crystallographica Section A*, **32**, 751 (1976).

14. E. J. Wu, P. D. Tepesch and G. Ceder, *Philos. Mag. B-Phys. Condens. Matter Stat. Mech. Electron. Opt. Magn. Prop.*, **77**, 1039 (1998).

15. K. Kang and G. Ceder, *Physical Review B (Condensed Matter and Materials Physics)*, **74**, 094105 (2006).

16. J. K. Ngala, N. A. Chernova, M. Ma, M. Mamak, P. Y. Zavalij and M. S. Whittingham, *Journal of Materials Chemistry*, **14**, 214 (2004).

17. M. Yoshio, H. Noguchi, J. Itoh, M. Okada and T. Mouri, *Journal of Power Sources*, **90**, 176 (2000).

18. A. Manthiram, J. Choi and W. Choi, *Solid State Ionics*, **177**, 2629 (2006).

19. K. S. Kang, Y. S. Meng, J. Breger, C. P. Grey and G. Ceder, *Science*, **311**, 977 (2006).

20. T. A. Hewston and B. L. Chamberland, *J. Phys. Chem. Solids*, **48**, 97 (1987).

21. J. N. Reimers, E. Rossen, C. D. Jones and J. R. Dahn, *Solid State Ionics*, **61**, 335 (1993).

22. Y. S. Meng, Y. W. Wu, B. J. Hwang, Y. Li and G. Ceder, *J. Electrochem. Soc.*, **151**, A1134 (2004).

23. S.-K. Hu, T.-C. Chou, B.-J. Hwang and G. Ceder, *Journal of Power Sources*, **160**, 1287 (2006).

24. M. Ganesan, S. Sundararajan, M. V. T. Dhananjeyan, K. B. Sarangapani and N. G. Renganathan, *Materials Science and Engineering: B*, **131**, 203 (2006).

25. H.-W. Ha, K. H. Jeong and K. Kim, *Journal of Power Sources*, **161**, 606 (2006).

26. M. Tsuda, H. Arai, M. Takahashi, H. Ohtsuka, Y. Sakurai, K. Sumitomo and H. Kageshima, *Journal of Power Sources*, **144**, 183 (2005).

27. H. Liu, J. Li, Z. Zhang, Z. Gong and Y. Yang, *Electrochim. Acta*, **49**, 1151 (2004).

28. H. Arai, M. Tsuda and Y. Sakurai, *Journal of Power Sources*, **90**, 76 (2000).

29. L. A. Chick, L. R. Pederson, G. D. Maupin, J. L. Bates, L. E. Thomas and G. J. Exarhos, *Materials Letters*, **10**, 6 (1990).

30. J. Wilcox and M. Doeff, *ECS Transactions*, **11**, 27 (2008).

31. C. H. Jung, J. Y. Park, S. J. Oh, H. K. Park, Y. S. Kim, D. K. Kim and J. H. Kim, *Journal of Nuclear Materials*, **253**, 203 (1998).

32. J. Rodriguez-Carvajal, *Physica B: Condensed Matter*, **192**, 55 (1993).

33. J. Choi and A. Manthiram, *J. Electrochem. Soc.*, **152**, A1714 (2005).

34. Y. W. Tsai, B. J. Hwang, G. Ceder, H. S. Sheu, D. G. Liu and J. F. Lee, *Chem. Mat.*, **17**, 3191 (2005).

35. S. Patoux, M. Dolle and M. M. Doeff, *Chem. Mater.*, **17**, 1044 (2005).

36. S. Albrecht, J. Kumpers, M. Kruft, S. Malcus, C. Vogler, M. Wahl and M. Wohlfahrt-Mehrens, *Journal of Power Sources*, **119**, 178 (2003).

37. J. K. Ngala and M. M. Natasha A. Chernova, Marc Mamak, Peter Y. Zavalij and M. Stanley Whittingham, *J. Mater. Chem.*, 214 (2004).

38. T. Ohzuku, K. Nakura and T. Aoki, *Electrochim. Acta*, **45**, 151 (1999).

39. M. Guilmard, A. Rougier, M. Grune, L. Croguennec and C. Delmas, *Journal of Power Sources*, **115**, 305 (2003).

40. G. Ceder, Y. M. Chiang, D. R. Sadoway, M. K. Aydinol, Y. I. Jang and B. Huang, *Nature*, **392**, 694 (1998).

41. J. P. Peres, C. Delmas, A. Rougier, M. Broussely, F. Perton, P. Biensan and P. Willmann, *J. Phys. Chem. Solids*, **57**, 1057 (1996).

42. C. Delmas, J. P. Peres, A. Rougier, A. Demourgues, F. Weill, A. Chadwick, M. Broussely, F. Perton, P. Biensan and P. Willmann, *Journal of Power Sources*, **68**, 120 (1997).

43. J. Choi and A. Manthiram, *Electrochemical and Solid-State Letters*, **8**, C102 (2005).

44. J. R. Mueller-Neuhaus, R. A. Dunlap and J. R. Dahn, *J. Electrochem. Soc.*, **147**, 3598 (2000).

45. S. Patoux and M. M. Doeff, *Electrochem. Commun.*, **6**, 767 (2004).

46. S. Buta, D. Morgan, A. Van der Ven, M. K. Aydinol and G. Ceder, *J. Electrochem. Soc.*, **146**, 4335 (1999).

47. M. Guilmard, C. Pouillerie, L. Croguennec and C. Delmas, *Solid State Ionics*, **160**, 39 (2003).

48. F. Zhou, X. Zhao, Z. Lu, J. Jiang and J. R. Dahn, *Electrochem. Commun.*, **10**, 1168 (2008).

49. F. Zhou, X. Zhao, Z. Lu, J. Jiang and J. R. Dahn, **11**, A155 (2008).

Figure Captions

Figure 1. SEM image of $LiNi_{1/3}Co_{1/3}Mn_{1/3}O_2$ powder produced via the glycine nitrate combustion method. Secondary particles with a diameters in the range of 500 nm are comprised of ~40-50 nm primary particles.

Figure 2. Powder XRD patterns of $LiNi_{1/3}Co_{1/4}M_{1/12}Mn_{1/3}O_2$ (M =Ti, Fe, Al, and Co). All materials were single phase and could be indexed to the $R\bar{3}m$ space group.

Figure 3. Discharge capacities of $Li/LiNi_{1/3}Co_{1/4}M_{1/12}Mn_{1/3}O_2$ (M=Ti, Fe, Al, and Co) cells. Cycling was limited to 2.0-4.3 V vs. Li/Li^+ at a constant charge and discharge current density of 0.1 mA/cm^2.

Figure 4. Differential capacity plots of the first cycles of $Li/LiNi_{1/3}Co_{1/4}M_{1/12}Mn_{1/3}O_2$ (M=Co, Ti, Al, and Fe) cells. Current density was 0.1 mA/cm^2 in the potential range 2.0-4.3 V vs. Li/Li^+.

Figure 5. Discharge capacities of $Li/LiNi_{1/3}Co_{1/4}M_{1/12}Mn_{1/3}O_2$ (M=Ti, Fe, Al, and Co) cells.. Cycling was limited to 2.0-4.7 V vs. Li/Li^+ at a constant charge and discharge current density of 0.1 mA/cm^2.

Figure 6. Rate capabilities of $Li/LiNi_{1/3}Co_{1/4}M_{1/12}Mn_{1/3}O_2$ (M=Ti, Fe, Al, and Co) cells . Cycling was limited to 2.0-4.3 V and a constant charge current density of 0.1 mA/cm^2 was used.

Figure 7. First cycles of $Li/LiNi_{1/3}Co_{1/4}M_{1/12}Mn_{1/3}O_2$ (M=Ti, Fe, Al, and Co) cells at 0.1 mA/cm^2 between 2.0 and 4.3 V vs. Li/Li^+. Irreversible capacities are defined in the text.

Figure 8. Powder XRD diffraction patterns of $LiNi_{1/3}Co_{1/3-x}Al_xMn_{1/3}O_2$, ($0 \leq y \leq 1/3$) compounds. All materials were single phase except y=1/3, in which an impurity of γ-$LiAlO_2$ (*) is observed. Insets show the consistent shift in the 003 peak and increased 018/110 peak splitting. This implies improved lamellar character with increased Al content.

Figure 9. Discharge capacities of $Li/LiNi_{1/3}Co_{1/3-x}Al_xMn_{1/3}O_2$, ($0 \leq y \leq 1/3$) cells. Cycling was limited to 2.0-4.3 V vs. Li/Li^+ at a constant charge and discharge current density of 0.1 mA/cm^2.

Figure 10. Differential capacity plots of the first cycles of $Li/LiNi_{1/3}Co_{1/3-x}Al_xMn_{1/3}O_2$, ($0 \leq y \leq 1/3$) cells. Current density was 0.1 mA/cm^2 in the potential range 2.0-4.3 V vs. Li/Li^+.

Figure 11. Discharge capacities of $Li/LiNi_{1/3}Co_{1/3-x}Al_xMn_{1/3}O_2$, ($0 \leq y \leq 1/3$) cells. Cycling was limited to 2.0-4.7 V vs. Li/Li^+ at a constant charge and discharge current of 0.1 mA/cm^2.

Figure 12. Rate capabilities of $Li/LiNi_{1/3}Co_{1/3-x}Al_xMn_{1/3}O_2$, ($0 \leq y \leq 1/3$) cells. Cycling was limited to 2.0-4.3 V and a constant charge current density of 0.1 mA/cm^2 was used.

Figure 13. Irreversible capacities of Li/$LiNi_{1/3}Co_{1/3-x}Al_xMn_{1/3}O_2$, ($0 \leq y \leq 1/3$ cells cycled to a charge cutoff potential of either 4.3 or 4.7 V (0.1 mA/cm^2 current density.

Table 1: Structural Parameters of $LiNi_{1/3}Co_{1/3-y}M_yMn_{1/3}O_2$ (M=Co, Ti, Fe, Al) compounds

Transition Metal	Substitution Level, y	Unit Cell Parameters		Unit Cell Volume (Å^3)	c/3a	z_{Ox}	*S* (MO_2) (Å)[a]	*I* (LiO_2) (Å)[a]
		a (Å)	c (Å)					
Co	1/12	2.862(2)	14.254(1)	101.145(2)	1.660	0.2574(2)	2.16	2.59
Ti	1/12	2.870(2)	14.298(2)	101.996(2)	1.661	0.2582(2)	2.15	2.62
Fe	1/12	2.873(3)	14.275(2)	102.072(2)	1.656	0.2590(2)	2.14	2.62
Al	1/12	2.862(2)	14.281(1)	101.332(2)	1.663	0.2596(2)	2.10	2.66
Al	1/6	2.863(2)	14.285(2)	101.423(2)	1.663	0.2593(2)	2.11	2.65
Al	1/4	2.863(2)	14.292(2)	101.437(2)	1.664	0.2590(2)	2.12	2.64
Al	1/3*	2.863(2)	14.298(2)	101.490(2)	1.665	0.2594(2)	2.11	2.66

a) Transition metal slab spacing (*S*) and lithium slab spacing (*I*) as defined in Ref.[47]

* γ-$LiAlO_2$ was observed as an impurity in this composition

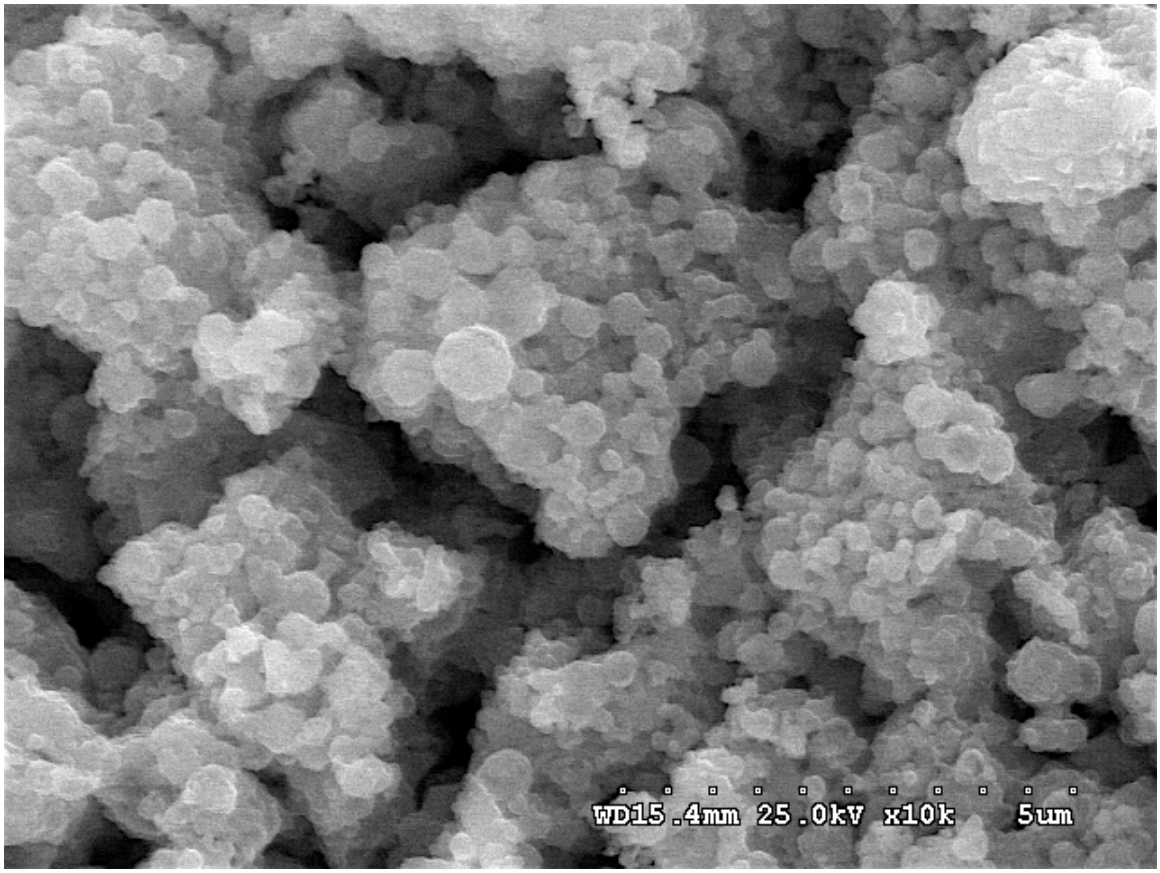

Figure 1

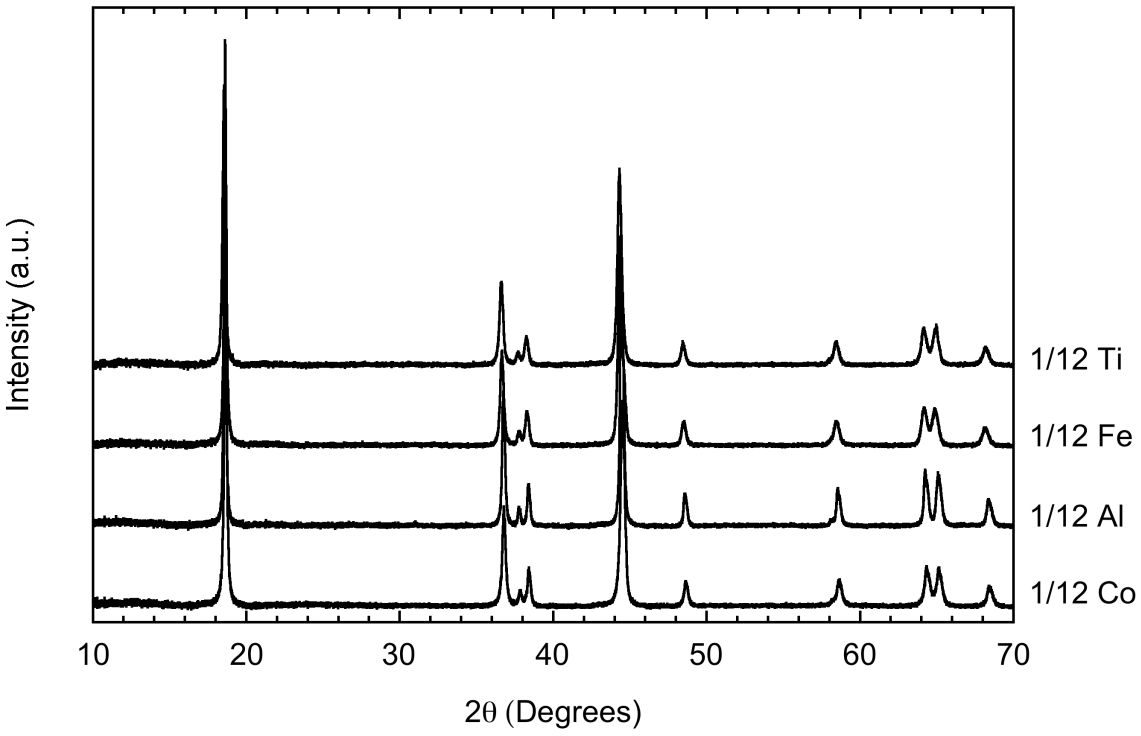
Intensity (a.u.)
1/12 Ti
1/12 Fe
1/12 Al
1/12 Co
10
20
30
40
50
60
70
2θ (Degrees)

Figure 2

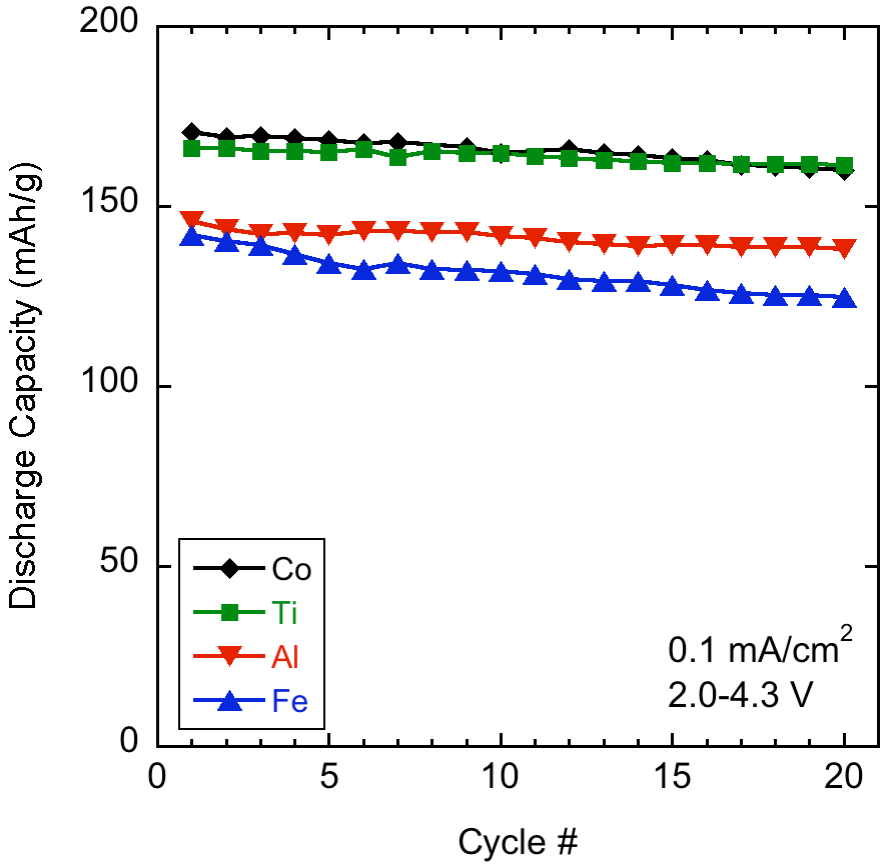
Discharge Capacity (mAh/g)
Cycle #
Co
Ti
Al
Fe
0.1 mA/cm2
2.0-4.3 V
0
50
100
150
200
0
5
10
15
20

Figure 3

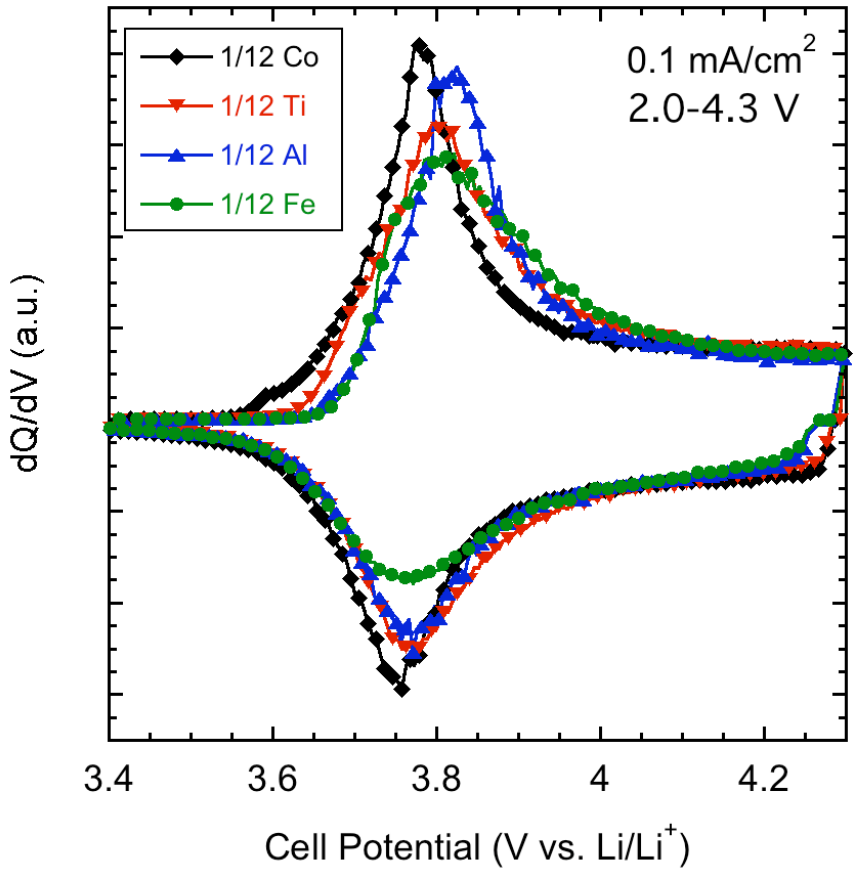
1/12 Co
1/12 Ti
1/12 Al
1/12 Fe
0.1 mA/cm2
2.0-4.3 V
dQ/dV (a.u.)
3.4
3.6
3.8
4
4.2
Cell Potential (V vs. Li/Li+)

Figure 4

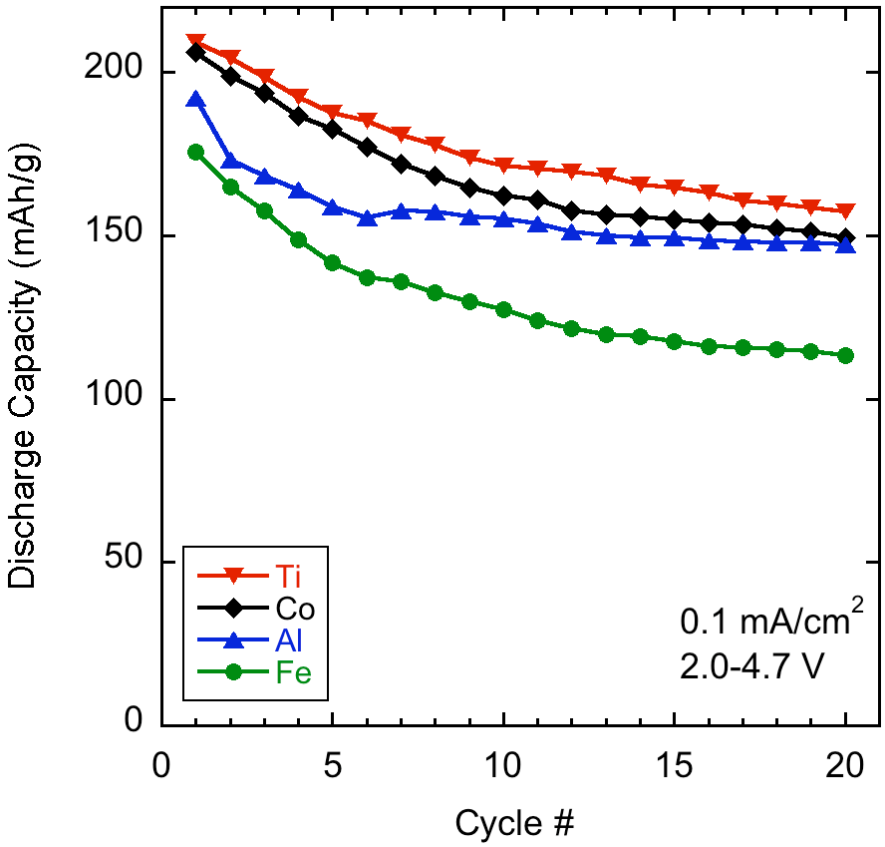
Discharge Capacity (mAh/g)
Cycle #
0
50
100
150
200
0
5
10
15
20
Ti
Co
Al
Fe
0.1 mA/cm2
2.0-4.7 V

Figure 5

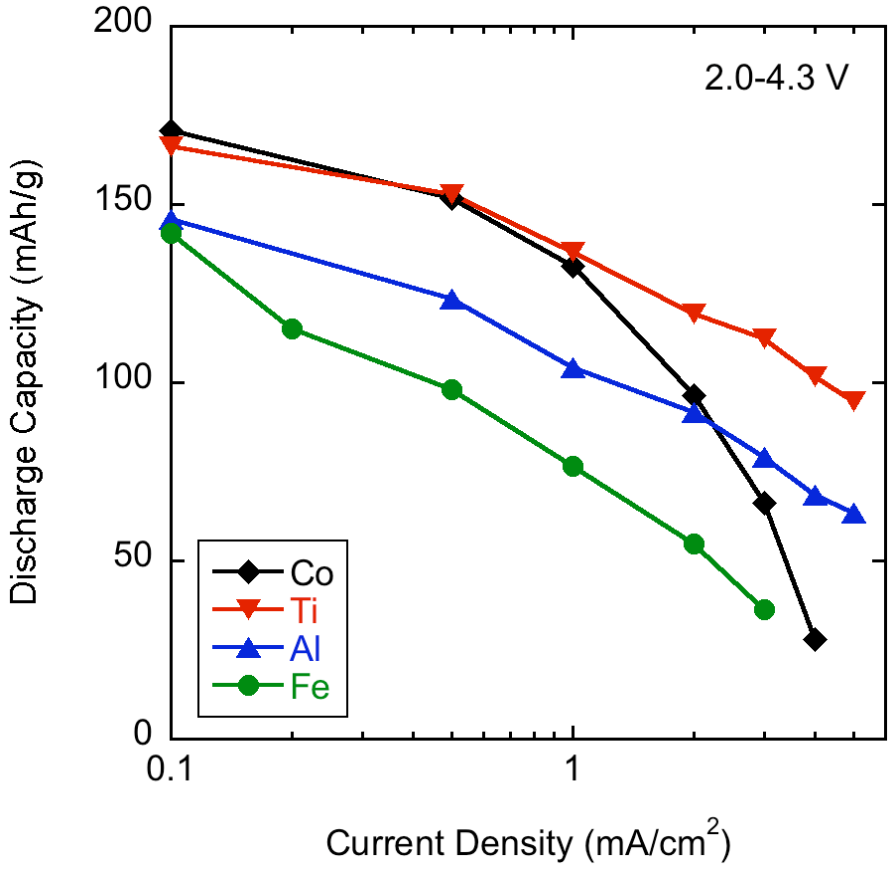
200
150
100
50
0
0.1
1
2.0-4.3 V
Co
Ti
Al
Fe
Discharge Capacity (mAh/g)
Current Density (mA/cm2)

Figure 6

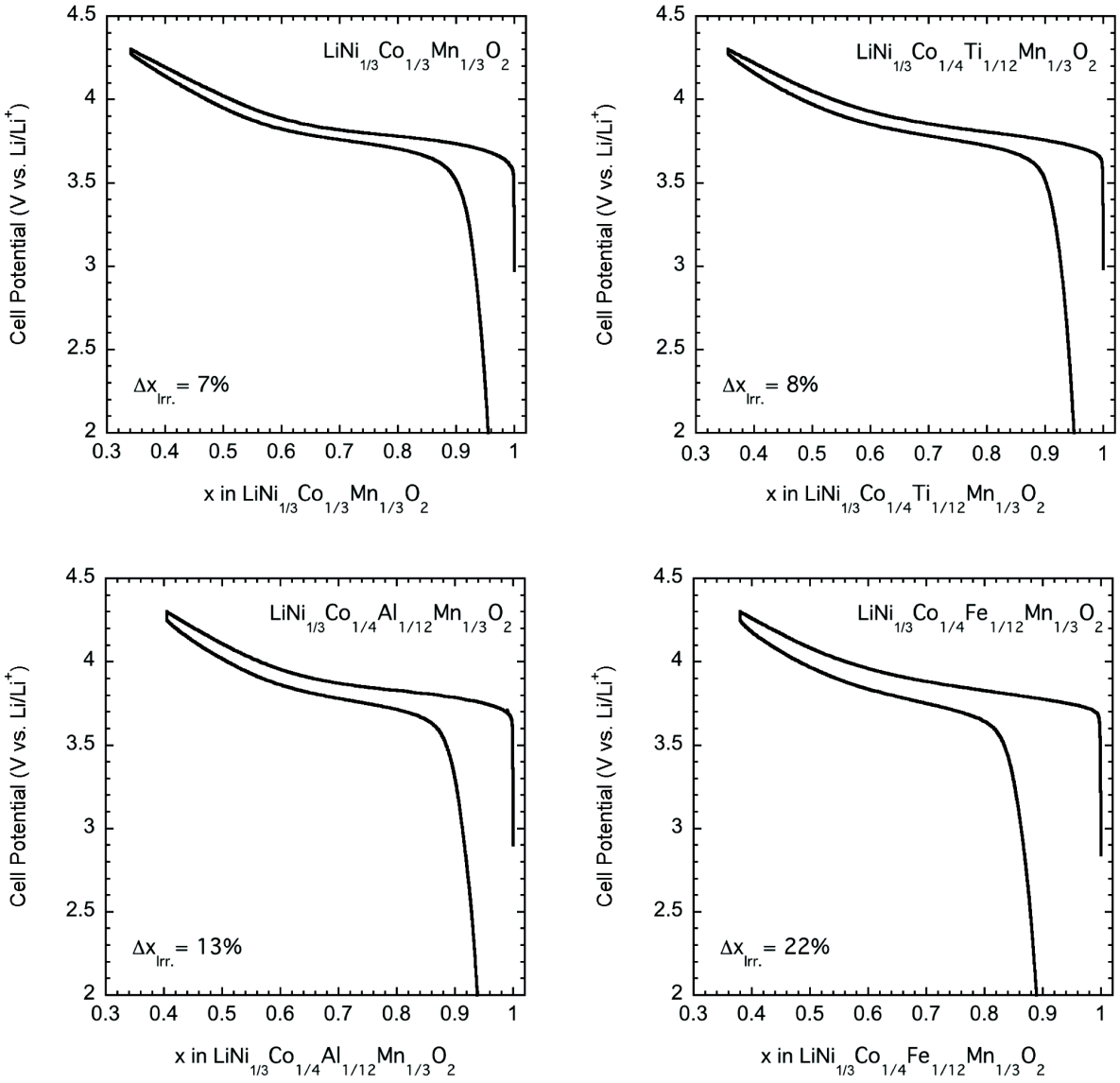
LiNi1/3Co1/3Mn1/3O2
Δxirr. = 7%
Cell Potential (V vs. Li/Li+)
x in LiNi1/3Co1/3Mn1/3O2
LiNi1/3Co1/4Ti1/12Mn1/3O2
Δxirr. = 8%
Cell Potential (V vs. Li/Li+)
x in LiNi1/3Co1/4Ti1/12Mn1/3O2
LiNi1/3Co1/4Al1/12Mn1/3O2
Δxirr. = 13%
Cell Potential (V vs. Li/Li+)
x in LiNi1/3Co1/4Al1/12Mn1/3O2
LiNi1/3Co1/4Fe1/12Mn1/3O2
Δxirr. = 22%
Cell Potential (V vs. Li/Li+)
x in LiNi1/3Co1/4Fe1/12Mn1/3O2

Figure 7

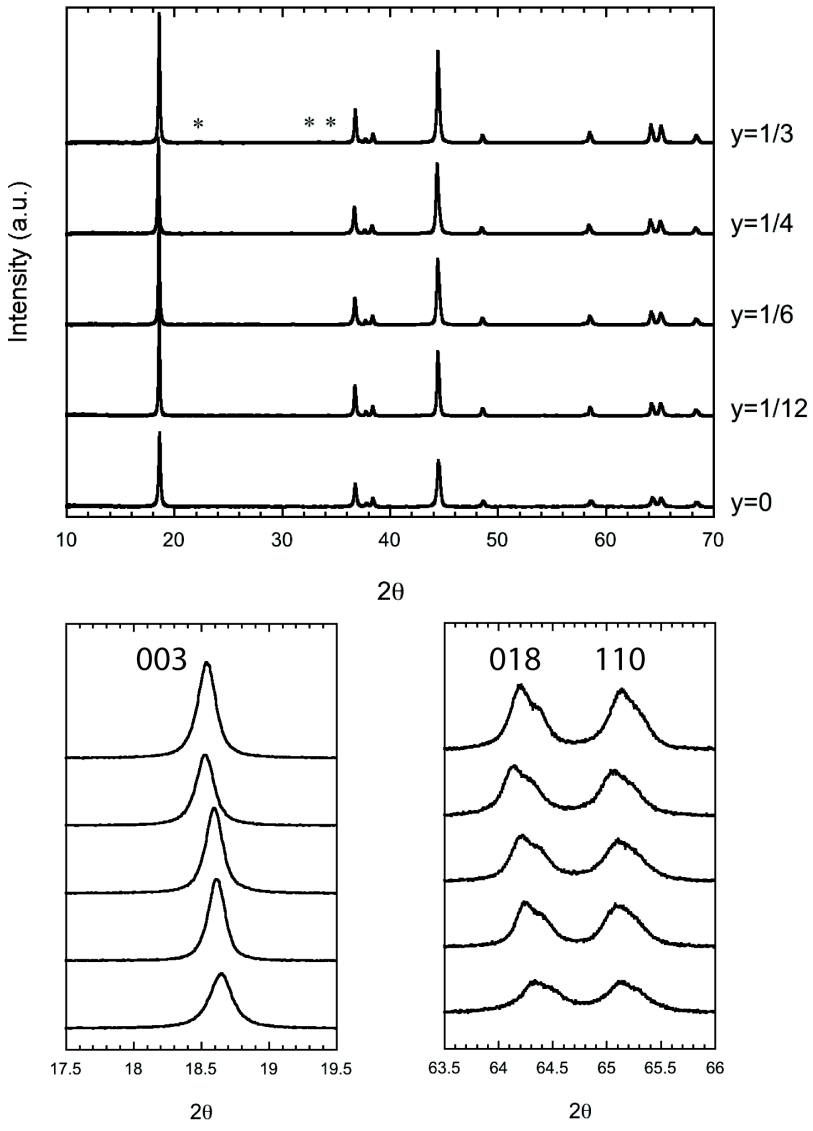
Intensity (a.u.)
y=1/3
y=1/4
y=1/6
y=1/12
y=0
*
* *
10
20
30
40
50
60
70
2θ
003
018
110
17.5
18
18.5
19
19.5
63.5
64
64.5
65
65.5
66
2θ
2θ

Figure 8

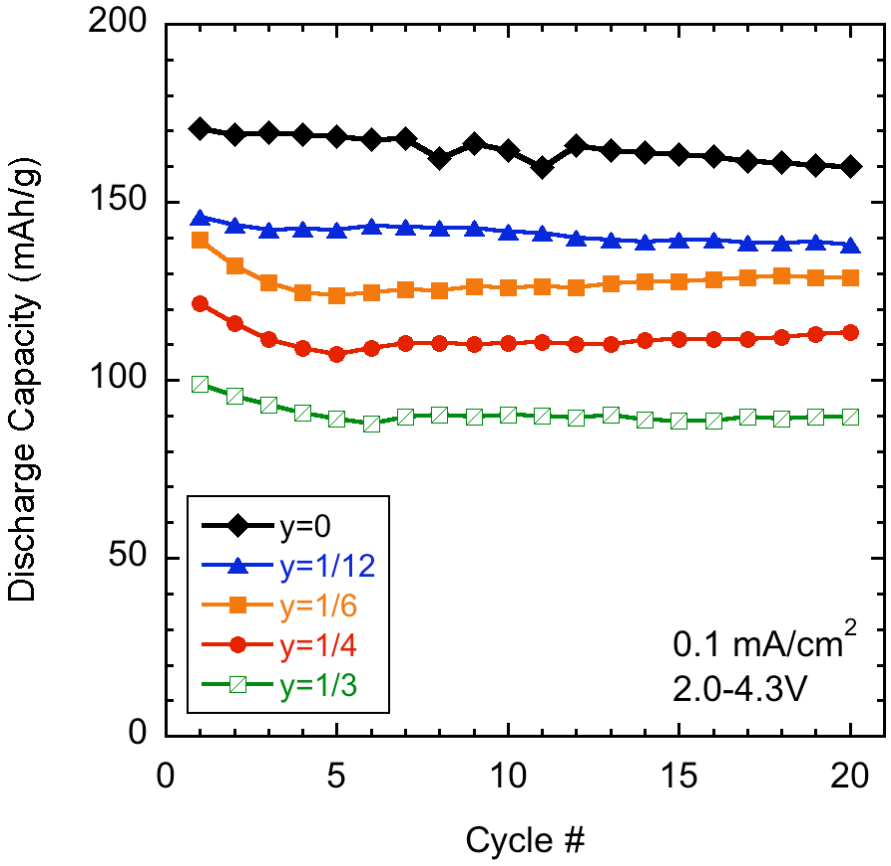
Discharge Capacity (mAh/g)
Cycle #
y=0
y=1/12
y=1/6
y=1/4
y=1/3
0.1 mA/cm2
2.0-4.3V
0
50
100
150
200
0
5
10
15
20

Figure 9

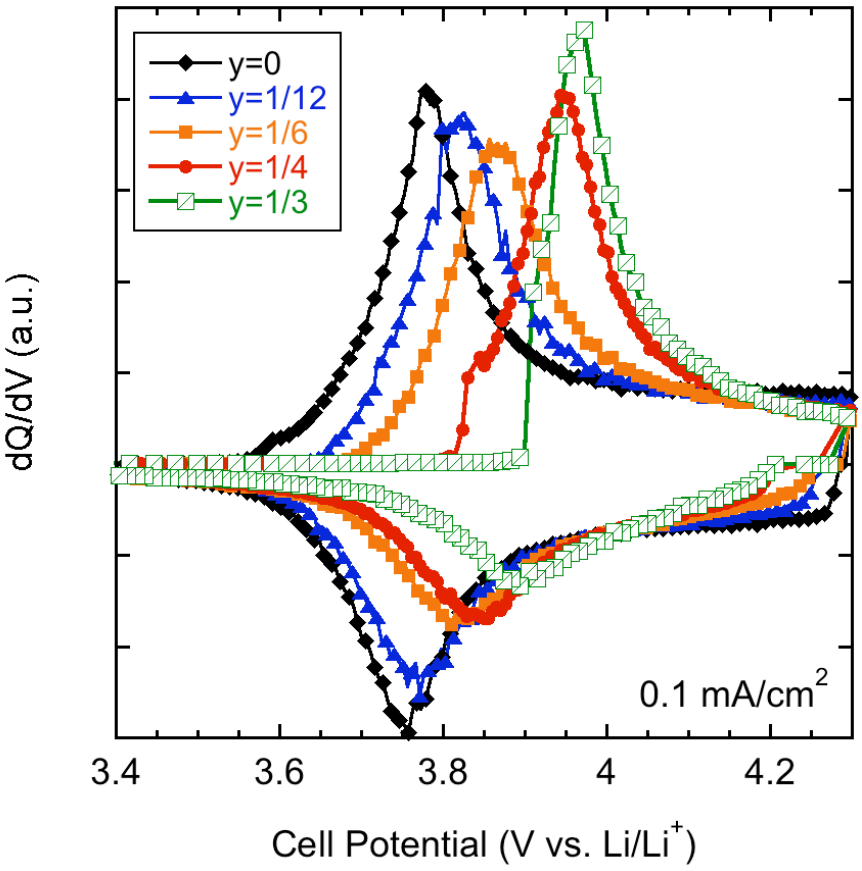
y=0
y=1/12
y=1/6
y=1/4
y=1/3
0.1 mA/cm2
dQ/dV (a.u.)
3.4
3.6
3.8
4
4.2
Cell Potential (V vs. Li/Li+)

Figure 10

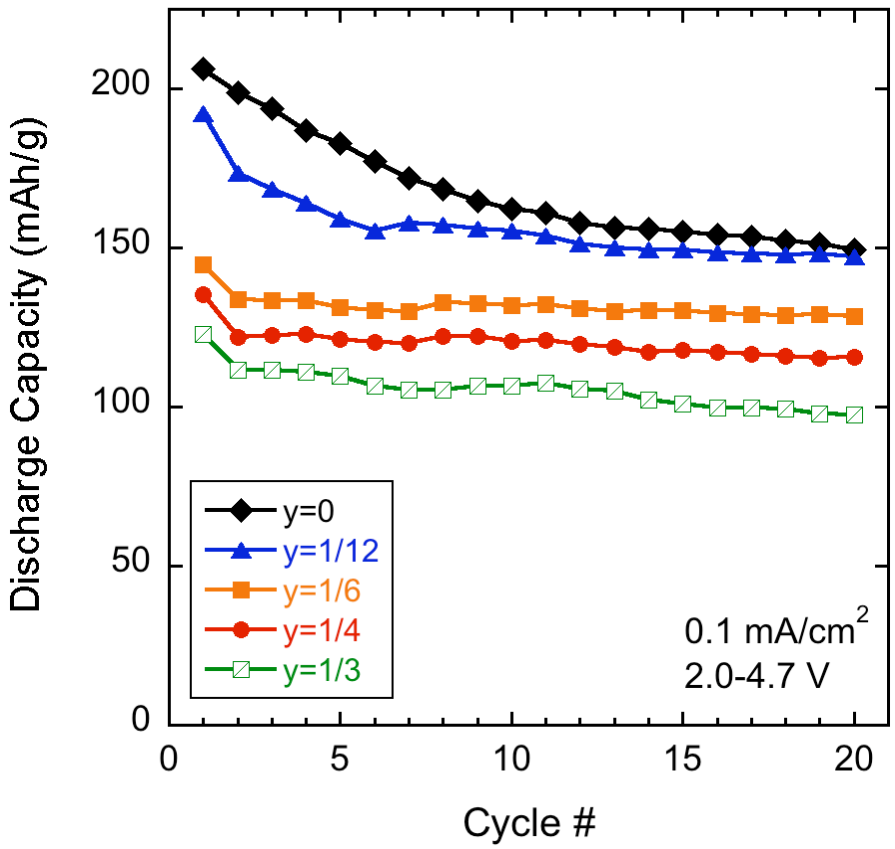
Discharge Capacity (mAh/g)
Cycle #
0
50
100
150
200
0
5
10
15
20
y=0
y=1/12
y=1/6
y=1/4
y=1/3
0.1 mA/cm2
2.0-4.7 V

Figure 11

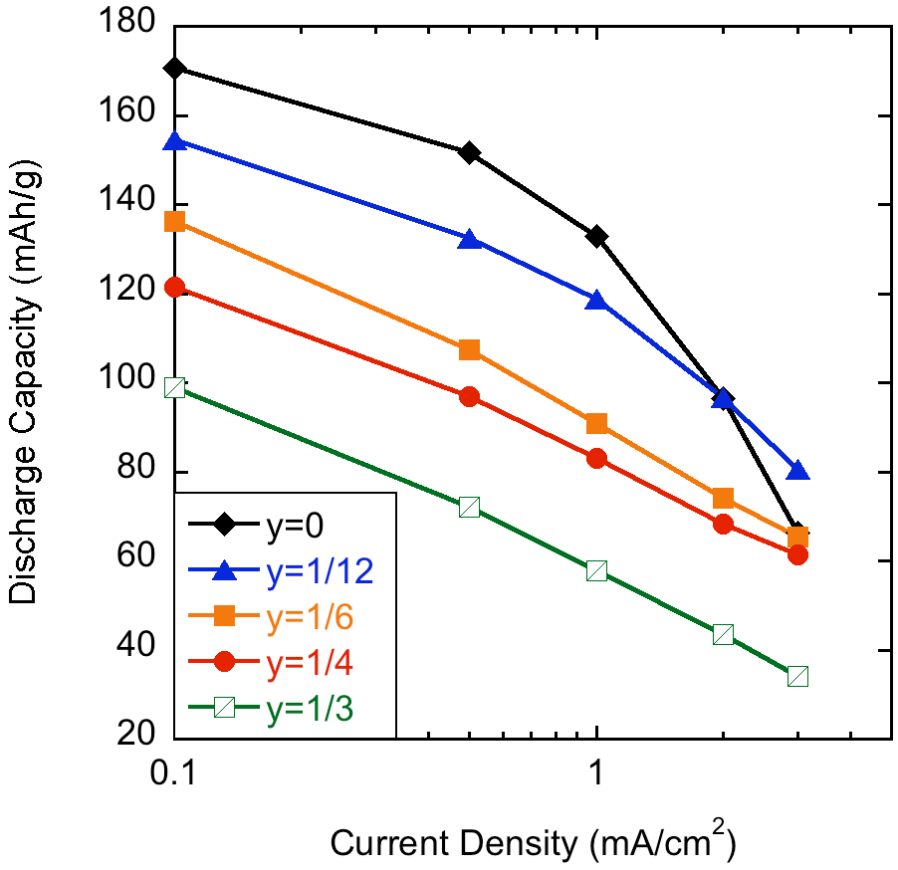
Discharge Capacity (mAh/g)
180
160
140
120
100
80
60
40
20
0.1
1
Current Density (mA/cm^2)
y=0
y=1/12
y=1/6
y=1/4
y=1/3

Figure 12

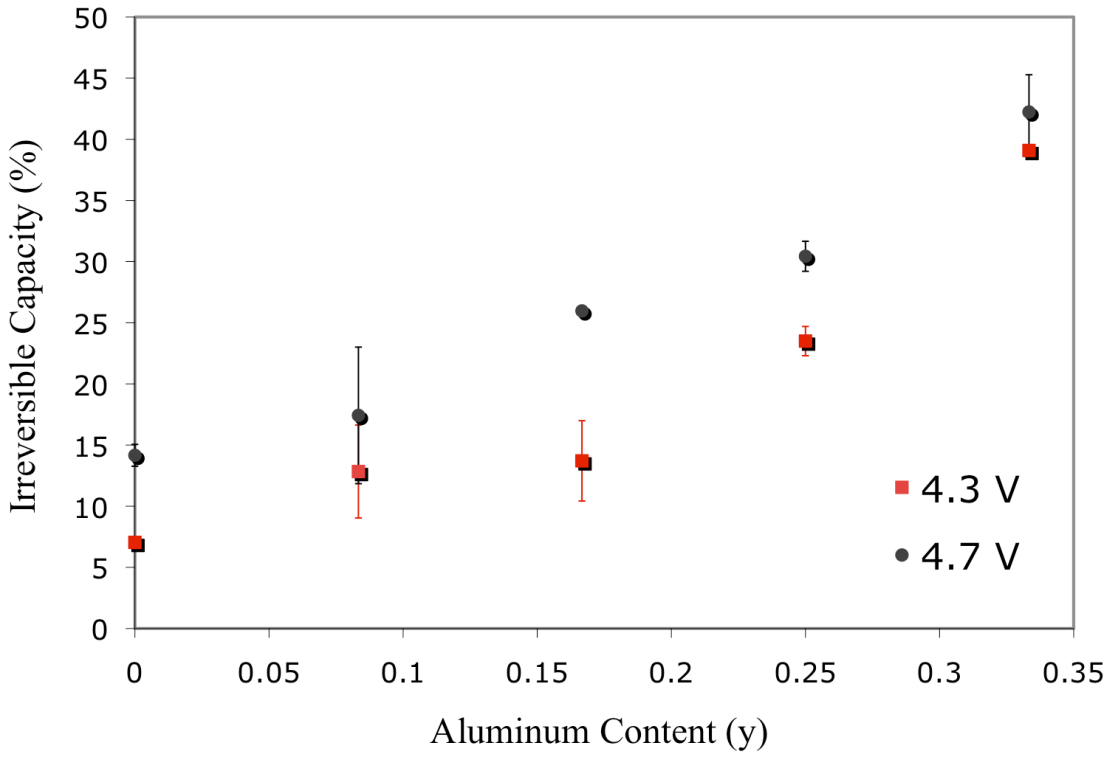
Irreversible Capacity (%)
50
45
40
35
30
25
20
15
10
5
0
0
0.05
0.1
0.15
0.2
0.25
0.3
0.35
Aluminum Content (y)
4.3 V
4.7 V

Figure 13